17th World Conference on Earthquake Engineering, 17WCEE
Sendai, Japan - September 13th to 18th 2020

Simulation of granular soil liquefaction due to Rayleigh wave transformation by 3D Discrete Element Method

M. Jiang[(1)], A. Kamura[(2)], M, Kazama [(3)],

[(1)] *Master course student, Tohoku University, jiang.mingjin.r1@dc.tohoku.ac.jp*
[(2)] *Assistant Professor, Tohoku University, akiyoshi.kamura.a4@tohoku.ac.jp*
[(3)] *Professor, Tohoku University, motoki.kazama.b2@tohoku.ac.jp*

Abstract

In the study of liquefaction problems, such as liquefaction mechanism and potential, cyclic loads applied to specimens in laboratory element tests correspond to primarily simple or pure shear conditions. However, earthquake loads are more complicated as opposed to simple or pure shear. Thus, it is necessary to understand the seismic behavior of ground materials under different seismic load types to understand the liquefaction mechanism in an earthquake. Surface waves, which consist of Love waves and Rayleigh waves, are important components in significant portions of strong ground motions.

The purpose of the study is to reveal the effect of Rayleigh waves on the liquefaction resistance of saturated granular material and its mechanism. The SHV-wave strain condition indicates that SH-waves travel vertically upward, and it is used as the control group. Initially, the strain governing equation of SHV-waves and Rayleigh waves were derived based on the theory of elastic waves and the strain–displacement relationship. The results indicated that the strains of soil elements under the Rayleigh wave excitation consist of two normal strains and one shear strain. Subsequently, a series of simulation tests under the SHV-wave strain condition and Rayleigh wave strain condition were performed via the 3D Discrete Element Method (DEM). Specifically, six specimens with states ranging from dense to loose were generated and K_0-consolidated. They were in almost the same initial stress state. Three cyclic load patterns were applied to the specimens. The shear strain amplitude under the SHV-wave strain condition was set as 2.5%. Two Rayleigh wave strain conditions, which are mainly different in the amplitude of shear strain, were considered, and their accumulated equivalent shear strain in a cycle were maintained identical to that under the SHV-wave strain conditions.

The results of the two Rayleigh wave strain conditions were almost identical. This implied that the normal strain, which relatively exceeds the shear strain at shallow depths that is liquefiable, corresponded to the dominant factor that affects the liquefaction behavior of specimens. The results were analyzed at the macro-scale and micro-scale. In the macroscale, the normalized accumulated dissipated energy (NDE) was used to evaluate the liquefaction potential of specimens under different strain conditions. In the microscale, the average coordination number was used to represent the stability of the structure system of specimens. The results indicated that in the same initial state and with the same accumulated equivalent shear strain in a cycle, the development of pore water pressure in specimens under the Rayleigh wave strain condition is considerably faster than that under the SHV-wave strain condition. Furthermore, liquefaction resistance of specimens under the Rayleigh wave strain condition was considerably lower than that under the SHV-wave strain condition. The reason is that it is easier to destroy the stable structure system of specimens in the Rayleigh wave strain condition.

Keywords: liquefaction, Rayleigh wave, 3D discrete element method

1. Introduction

Following the 1964 Alaska earthquake and 1964 Niigata earthquake, engineers and researchers increasingly concerned about the devastating effects of soil liquefaction. Thus, extensive studies focused on the liquefaction problem. Extant studies mainly focused on the physical properties of soils such as relative density, degree of saturation, and fine content. Given the limitation of laboratory test technology, cyclic loads applied to specimens in laboratory element tests are primarily simple or pure shear conditions. However, earthquake loads are more complicated than just simple or pure shear conditions. A comprehensive understanding of the seismic behavior of ground materials under different seismic load types is important to essentially determine the liquefaction mechanism.

There are two types of seismic waves in an earthquake: body waves and surface waves. Body waves are further divided into P-waves and S-waves. Surface waves constitute significant portions of strong ground motions [1] and consist of Love waves and Rayleigh waves. Generally, the liquefaction problem of level ground is assumed as caused by S-waves (shear waves) [2]. However, Fang, et al. (1979) analyzed aerial photographs over the sites of sand boil after the 1976 Tangshan Earthquake and suggested that some typical trace of liquefaction are induced by surface waves [3]. Subsequently, it was revealed that the surface waves correspond to a factor that lead to or aggravate the liquefaction of soils [4-7]. However, the studies only established a direct link between liquefaction problem and surface waves, and thus the liquefaction behaviors of ground materials under the surface wave strain conditions are not adequately understood to date. Love waves generate multi-directional shear stress in a medium. To clarify the effect of Love waves on the liquefaction resistance of saturated sands and its mechanism, Jiang et al. (2019) conducted a series of simulation tests via 3D discrete element method (DEM) and revealed that K_0-consolidated saturated specimen under Love wave strain condition are more prone to liquefy than under S-waves strain condition at the same shear strain amplitude [8]. Cui et al. (2004) noted that sand liquefaction and sand boil can be induced by either shear waves or by pressure waves [5]. Rayleigh waves are generated by the interference of P-waves and SV-waves, and they simultaneously generate normal stress and shear stress in a medium, which is more likely to induce liquefaction when compared with only shear waves or pressure wave loads [9].

The purpose of the study is to reveal the effect of Rayleigh waves on the liquefaction resistance of saturated granular material and its mechanism. It is difficult to reproduce the complicated strain condition of Rayleigh waves in a laboratory element test, and thus 3D DEM was utilized in the study. Specifically, DEM is a powerful tool to simulate the behavior of granular materials and was initially proposed by Cundall and Strack in 1979 [10-12]. It was developed from 2D to 3D and can reproduce the complicated stress/strain condition of soil elements while allowing observation at particle scales [13].

Two types of seismic wave loads that represent SHV-wave strain condition and Rayleigh wave strain condition were applied to the numerical specimens in 3D DEM. Their deformation modes are significantly different from each other. Normalized accumulated dissipated energy (NDE) was adopted to represent the liquefaction resistance of specimens under the two strain conditions. It is based on the energy concept and is effective in assessing liquefaction potential. Additionally, it also accommodates non-uniform loadings [14-16], which is applicable in the comparison between the SHV-waves strain condition and Rayleigh wave strain condition. After simulation tests, the liquefaction behavior of specimens under two strain conditions was analyzed, and the effect of Rayleigh waves on the liquefaction resistance of specimens was evaluated via NDE. Additionally, the liquefaction mechanism of specimens under the Rayleigh wave strain condition was discussed at a microscale level.

2. Strain governing equation

In the study, the strain applied to numerical specimen in 3D DEM are obtained from elastic wave theory. Specifically, theories and displacement governing equation are cited and summarized from *Elastic wave propagation and generation in seismology* [17].

2.1 SHV-wave strain condition

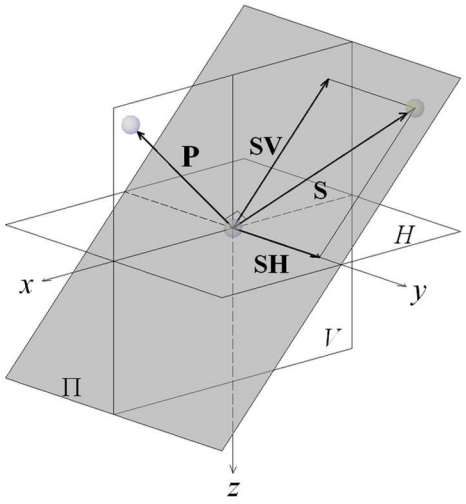

Fig. 1 – Direction of particle motions of S-waves and P-waves

A rectangular coordinate system and schematic of particle motions of S-waves and P-waves are shown in Fig.1. Specifically, S-waves are further divided into SH-waves and SV-waves in terms of the direction of particle motion. The particle motion of S-waves is parallel to the wavefront Π. The particle motion component corresponding to the SH-waves is in intersection Π of the horizontal plane (x, y) that is labeled H. The particle motion component corresponding to the SV-waves is in intersection Π of the vertical plane (x, z) that is labeled V.

In geotechnical engineering, S-waves are always assumed to travel vertically upward. Given the assumption, only SHV-wave strain condition (which indicates that SH-waves propagate vertically upward) was used as the control experiment of Rayleigh waves strain condition in the study. The S-wave travels perpendicular to the wavefront Π, and thus the displacement governing equation of SHV-waves is simplified as follows:

$$\boldsymbol{u}_{\mathrm{SHV}} = A\boldsymbol{a}_y \cos(\omega t - kz) \tag{1}$$

where $\boldsymbol{u}_{\mathrm{SHV}}$ denotes the displacement vector of SHV-waves; A denotes a constant; $\boldsymbol{a}_y$ denotes unit vectors along the y-axis; ω denotes angular frequency; t represents time; k denotes the wavenumber; and z denotes the coordinate of the particle in z-axis. The relationship between the displacement field and strain is shown below:

$$\varepsilon_{ij} = \frac{\partial \boldsymbol{u}_i}{\partial j} \tag{2}$$

where i and j range from x to z. The strain governing equation of SHV-waves is given as follows:

$$\gamma_{yz}(\mathrm{SHV}) = \frac{\partial \boldsymbol{u}_{\mathrm{SHV}}}{\partial z} = Ak \sin(\omega t - kz) \tag{3}$$

The results indicate that under the SHV-wave strain condition, the soil element only suffers from a cyclic shear strain load in the vertical plane, and this is in the form of sine waves.

2.2 Rayleigh wave strain condition

In the study, Rayleigh waves are assumed to travel along the surface of a homogenous half-space. The motion of Rayleigh waves is a combination of P-waves and SV-waves motion. As shown in Fig.1, the results indicate that the particle motion is perpendicular to the wavefront Π. Furthermore, the combination motion can be solved as a plane problem. The Rayleigh wave is assumed to occur in xz-plane and travels along x-axis. The

origin of the coordinate is located on the surface of the medium. Thus, the displacement governing equation of Rayleigh waves is given as follows:

$$\boldsymbol{u}_{\mathrm{R}} = \left[B(\boldsymbol{a}_x - \mathrm{i}\gamma_\alpha \boldsymbol{a}_z)\mathrm{e}^{-\gamma_\alpha kz} + C\left(\mathrm{i}\gamma_\beta \boldsymbol{a}_x + \boldsymbol{a}_z\right)e^{-\gamma_\beta kz}\right]\mathrm{e}^{\mathrm{i}k(ct-x)} \tag{4}$$

where $\boldsymbol{u}_{\mathrm{R}}$ denotes displacement vectors of SHV-waves; B and C denote constants; $\boldsymbol{a}_x$ and $\boldsymbol{a}_z$ denote the unit vectors along the x and z-axis, respectively; i denotes an imaginary unit; e denotes Napier's constant; c denotes the velocity of Rayleigh waves; x denotes the coordinate of particle in x-axis; and γ_α *and* γ_β are defined as follows:

$$\begin{cases} \gamma_\alpha = \sqrt{1 - c^2/\alpha^2} \\ \gamma_\beta = \sqrt{1 - c^2/\beta^2} \end{cases} \tag{5}$$

where α and β denote the velocity of P-waves and SV-waves, respectively.

There are boundary conditions that Rayleigh waves should satisfy, and thus the velocity of Rayleigh waves in the medium depends on the velocity of P-waves and SV-waves. The displacement of Rayleigh waves approaches zero when z approaches infinity. Therefore, c must be lower than δ. The stress across the surface of the medium should correspond to zero. Thus, the following equation must be satisfied:

$$\left(2 - \frac{c^2}{\beta^2}\right)^2 - 4\gamma_\alpha\gamma_\beta = 0 \tag{6}$$

The velocity of Rayleigh waves in the medium are calculated when the velocities of P-waves and SV-waves are given.

We rewrite Eq. (4) in scalar form, and the displacement governing equation of Rayleigh waves is expressed as follows:

$$\begin{cases} u_x = Q\left[\mathrm{e}^{-\gamma_\alpha kz} - \left(1 - \dfrac{c^2}{2\beta^2}\right)\mathrm{e}^{-\gamma_\beta kz}\right]\sin(\omega t - kx) \\ u_z = Q\gamma_\alpha\left[-\mathrm{e}^{-\gamma_\alpha kz} + \left(1 - \dfrac{c^2}{2\beta^2}\right)^{-1}\mathrm{e}^{-\gamma_\beta kz}\right]\cos(\omega t - kx) \end{cases} \tag{7}$$

where u_x and u_z denote the displacement of Rayleigh waves along x- and z-axes; and Q denotes a constant. The strain governing equation of Rayleigh waves is derived from Eq. (7) and is shown below:

$$\begin{cases} \varepsilon_x(R) = \dfrac{\partial u_x}{\partial x} = -Qk\left[\mathrm{e}^{-\gamma_\alpha kz} - \left(1 - \dfrac{c^2}{2\beta^2}\right)\mathrm{e}^{-\gamma_\beta kz}\right]\cos(\omega t - kx) \\ \varepsilon_z(R) = \dfrac{\partial u_z}{\partial z} = Qk\gamma_\alpha\left[\gamma_\alpha\mathrm{e}^{-\gamma_\alpha kz} - \gamma_\beta\left(1 - \dfrac{c^2}{2\beta^2}\right)^{-1}\mathrm{e}^{-\gamma_\beta kz}\right]\cos(\omega t - kx) \\ \gamma_{xz}(R) = \dfrac{\partial u_x}{\partial z} + \dfrac{\partial u_z}{\partial x} = Qk\left\{-2\gamma_\alpha\mathrm{e}^{-\gamma_\alpha kz} + \left[\gamma_\beta\left(1 - \dfrac{c^2}{2\beta^2}\right) + \gamma_\alpha\left(1 - \dfrac{c^2}{2\beta^2}\right)^{-1}\right]\mathrm{e}^{-\gamma_\beta kz}\right\}\sin(\omega t - kx) \end{cases} \tag{8}$$

From Eq. (8), the results indicate that the strain of Rayleigh waves consists of two normal strains and a shear strain. The amplitude of each strain component is affected by the velocity of waves and by the depth from the surface of the medium.

In the study, saturated granular soil is assumed as undrained during cyclic loads. Therefore, the volume

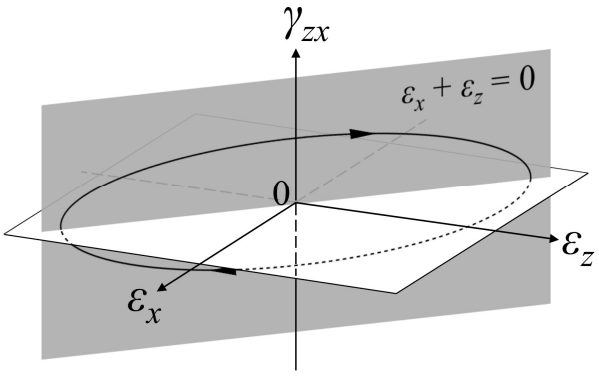

Fig. 2 – Load path under Rayleigh wave strain condition (in case of Rayleigh wave strain condition II)

of a soil element in the homogenous elastic medium should be constant, and this indicates that the bulk modulus of the medium approaches infinity. The velocity of P-waves is given as follows:

$$\alpha = \sqrt{(K + 4/3\mu)/\rho} \tag{9}$$

where K denotes bulk modulus; μ denotes Lamé's second parameter; and ρ denotes the density of the medium. Hence, the velocity of P-waves approaches infinity. In the condition, the normal strain amplitude in the x-direction corresponds to that in the z-direction as shown in the load path in Fig.2. Specifically, ε_x and ε_z are equal in absolute value and opposite in sign. In the study, the compaction direction is specified as positive. Additionally, a phase difference of $\pi/2$ exists between the normal strain component and shear strain component.

We assume that the velocity of SV-waves is 150 m/s, and the period of Rayleigh waves is 6 s. At a depth of 2 m, the ratio of normal strain amplitude to shear strain amplitude corresponds to 21.78. At a depth of 10 m, the ratio of normal strain amplitude to shear strain amplitude corresponds to 4.05. Specifically, in the aforementioned condition, the normal strain relatively exceeds the shear strain at shallow depths that is liquefiable, which is typically below 15 m.

3. Simulation tests

The simulation tests were conducted via the commercial code Rocky 4. To improve the calculation efficiency, only single-sized particles were used. Six specimens were generated, and their void ratio ranged from 0.80 to 0.75, which represents a state from loose to dense. Specifically, particles were initially generated from an inlet and uniformly fell to a space that was constrained by six frictionless rigid walls. The size of the cuboid space corresponded to 100 mm × 100 mm × 200 mm. The square inlet was below the upper boundary wall and exhibited a size of 100 mm. Subsequently, the upper boundary wall was moved vertically downward at a speed

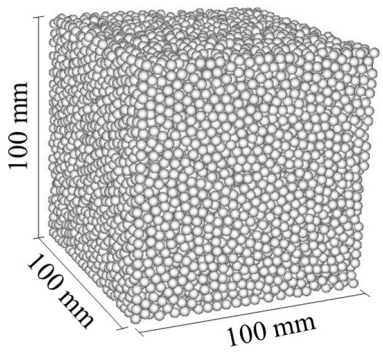

Fig. 3 – Generated specimen

of 2 mm/s to compact the specimens in K_0-condition. The final size of specimens is 100 mm × 100 mm × 100 mm as shown in Fig.3. To bring the specimens with different void ratios to almost the same initial stress state, their initial rolling resistance coefficient was different. Finally, the rolling resistance coefficients of the specimens were uniformly adjusted to 0.35. The parameters in the simulation tests are shown in Table 1. The particle number and initial stress state of specimens are shown in Table 2, where σ'_x, σ'_y, and σ'_z denotes the effective normal stress in each direction.

Table 1 – Parameters in the 3D DEM simulation

Particles	
Diameter (mm)	4
Density (g/cm^3)	2.667
Elastic modulus (N/m^2)	1.0×10^7
Boundary walls	
Elastic modulus (N/m^2)	1.0×10^{11}
Interactions	
Coefficient of restitution	0.3
Tangential stiffness ratio	1
Friction coefficient (particle/particle)	0.7
Friction coefficient (particle/boundary)	0.0
Rolling resistance coefficient	0.35
Computational parameters	
Time step (s)	5.0×10^{-6}

Table 2 – Particle number and initial stress state of the given specimens

Void ratio	Particle number	σ'_x (kPa)	σ'_y (kPa)	σ'_z (kPa)	K_0
0.80	16579	13.99	13.97	32.58	0.43
0.79	16672	14.12	14.21	32.20	0.44
0.78	16765	13.84	14.11	31.94	0.44
0.77	16860	14.03	13.87	31.98	0.44
0.76	16956	14.05	13.99	31.85	0.44
0.75	17053	14.05	14.41	31.62	0.45

In the study, the interaction model between particles and particles or between particles and boundaries consisted of three parts: normal force model, tangential force model, and rolling resistance model. Specifically, the normal force model corresponded to linear spring dash model, which is simplified as a parallel connection of a linear spring and viscous dashpot. The tangential force model corresponded to a linear spring Coulomb limit model, which is idealized as a connection of a linear spring and slider in series. The rolling resistance model is represented by a connection of a rotation spring and rotation slider in series.

The constant volume method was used to simulate the undrained condition. The method was based on the assumption that water is incompressible and the volume of samples in DEM is constant. However, in natural saturated soil, the free particles that lost contact with other particles are suspended for the drag of the pore fluid [18]. There was no fluid model in the simulation performed via the constant volume method. Conversely, the gravity in the simulation was set as zero.

Two types of cyclic loads were applied to the specimens via the cyclic motion of boundary walls. The cyclic loads represent the SHV-wave strain condition and Rayleigh wave strain condition. The motion of boundary walls in simulation tests are shown in Fig.4. Two Rayleigh wave strain conditions were applied to the specimens to examine the effect of relative shear strain amplitude. When the ratio of normal strain amplitude to the shear strain amplitude corresponded to 21.78, the Rayleigh wave strain condition was termed

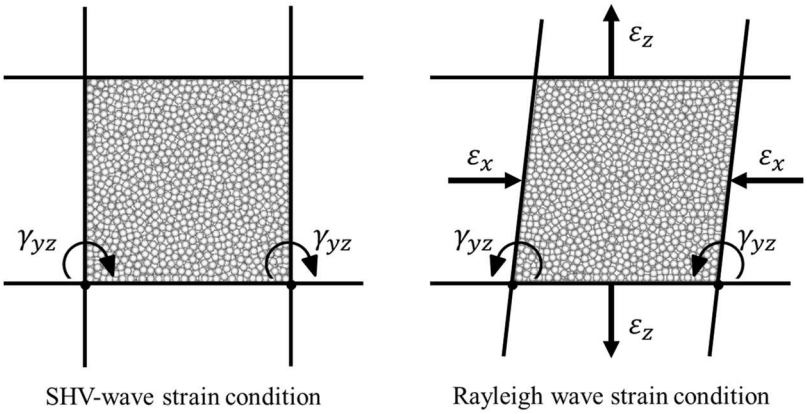

Fig. 4 – Motions of boundary walls at the initial time

as Rayleigh wave strain condition I and simplified as Rayleigh I. The Rayleigh wave strain condition with a ratio of normal strain amplitude to shear strain amplitude corresponding to 4.05 was termed as Rayleigh wave strain condition II and simplified as Rayleigh II in the study.

Accumulated equivalent shear strain in a cycle is seen as an invariant and is defined as follows:

$$\varepsilon^* = \sum_{n=0}^{T/\Delta t} \sqrt{\frac{4}{3}\Delta J_{2\varepsilon}(\varphi)} \tag{10}$$

where ε^* denotes the accumulated equivalent shear strain in a cycle; T denotes the period of the cyclic load; Δt denotes the time step; φ denotes the phase of cyclic load at time t; and $\Delta J_{2\varepsilon}(\varphi)$ denotes increases in the second deviatoric strain invariant when the phase is φ. In the study, ε^* in different strain conditions were maintained as identical. The half amplitude of shear strain under the SHV-wave strain condition was set as 2.5%. Correspondingly, under the Rayleigh wave strain condition I, the half amplitude of normal strain corresponded to 1.248% and the half amplitude of shear strain corresponded to 0.057%. Under the Rayleigh wave strain condition II, the half amplitude of normal strain corresponded to 1.222% and the half amplitude of shear strain corresponded to 0.302%. Additionally, all the cyclic loads were applied to the specimens at a frequency of 5 Hz.

4. Results

4.1 Development of excess pore water pressure

The development of excess pore water pressure is an important symbol during the liquefaction process. In the study, the excess pore water pressure ratio EPWPR is used to represent the relative value of excess pore water pressure and is defined as follows:

$$\mathrm{EPWPR} = 1 - \frac{\sigma'_{\mathrm{m}}}{\sigma'_{\mathrm{m,0}}} \tag{11}$$

where $\sigma'_{\mathrm{m,0}}$ denotes the initial mean effective stress, and σ'_{m} denotes the mean effective stress.

The maximum excess pore water pressure ratio inside specimens in each cycle is shown in Fig. 5. Generally, excess pore water pressure in dense specimens develops faster than that in loose specimens. The results also indicate that the development of pore water pressure in specimens under the Rayleigh wave strain condition significantly exceeds that under the SHV-wave strain condition. Specifically, in the initial cycle, the

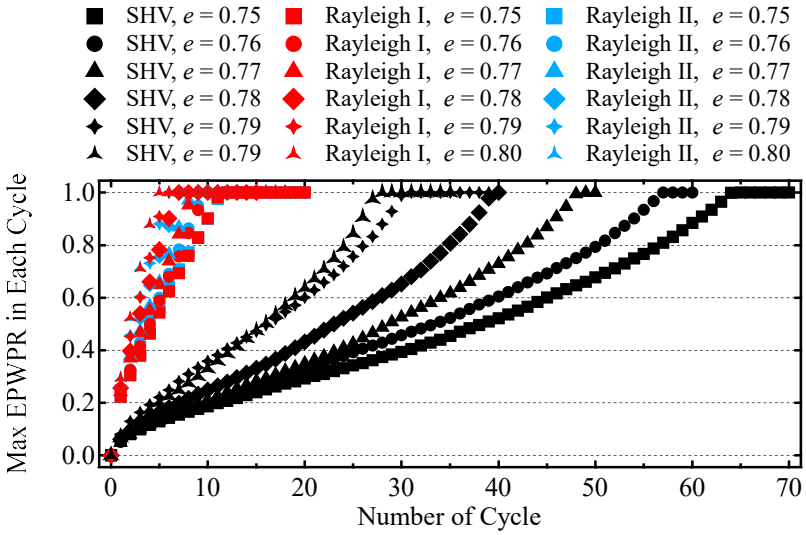

Fig. 5 – Development of excess pore water pressure in specimens

maximum EPWPR of specimens under the Rayleigh wave strain condition reaches 0.2. All specimens were liquefied under the SHV-wave strain condition and Rayleigh wave strain conditions, which were represented by EPWPR approaching 1. The development of excess pore water pressure under Rayleigh I and Rayleigh II is almost identical. This can be explained by the fact that the shear strain amplitude under two Rayleigh wave strain conditions is very low when compared to the normal strain amplitude. The relatively large normal strain corresponds to the dominant factor that affects the development of excess pore water pressure under the Rayleigh wave strain condition.

4.2 Mean effective stress during cyclic loads

During cyclic loads, the mean effective stress does not decrease to zero. In the study, the initial liquefaction is defined when the mean effective stress reaches 0.1 kPa, as shown in Fig.6. Furthermore, as also shown in Fig.6, the peak of the mean effective stress under the Rayleigh wave strain condition initially significantly increases.

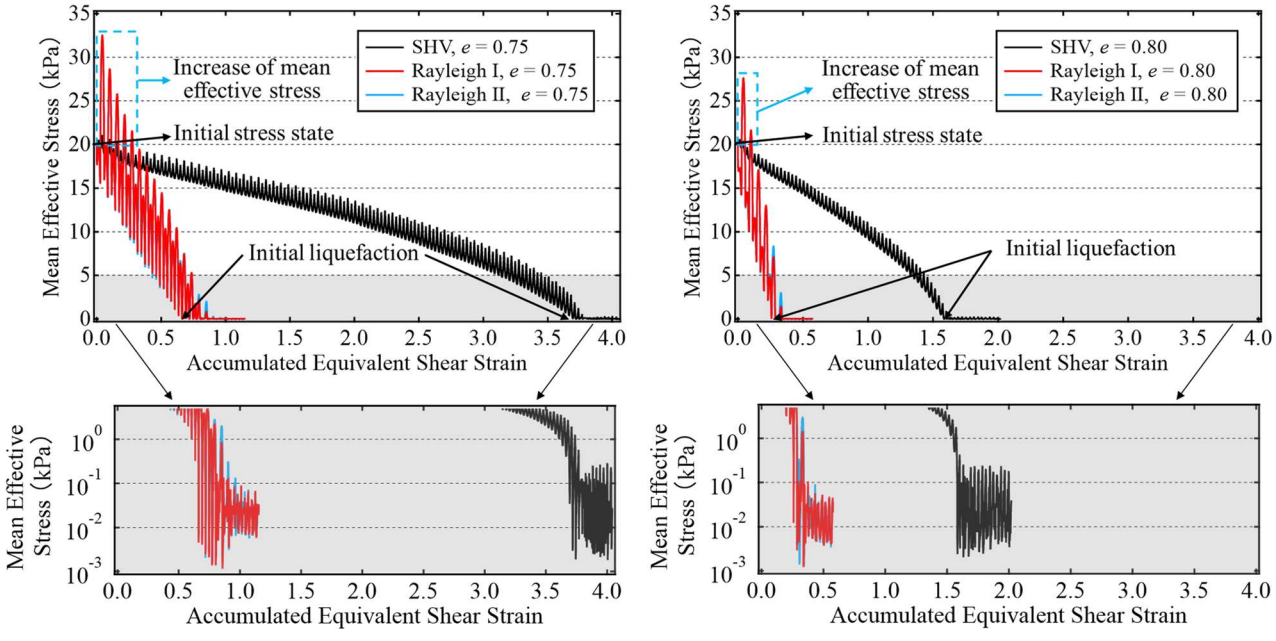

Fig. 6 – Mean effective stress of specimens with void ratios of 0.75 and 0.80 during cyclic loads

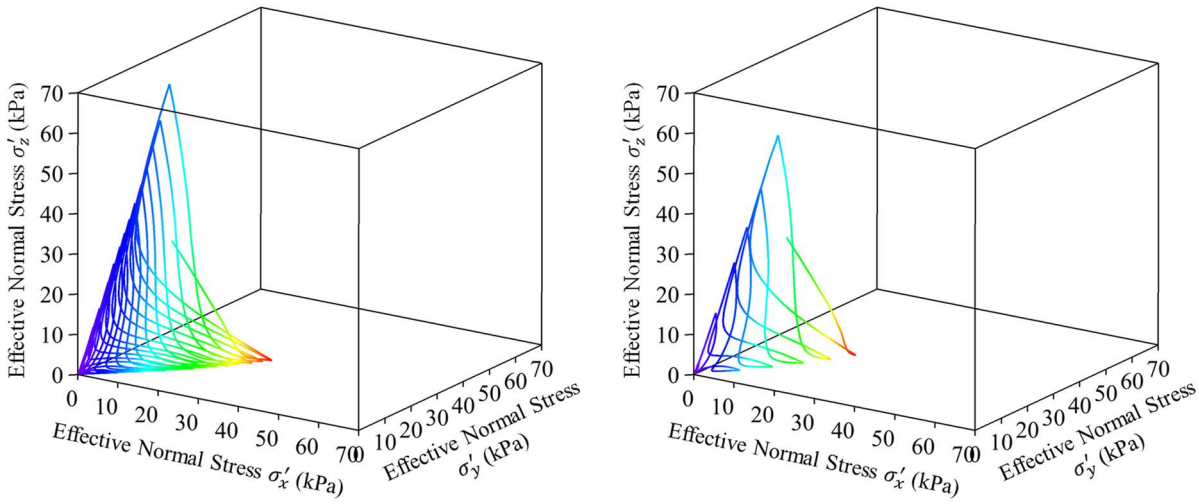

Fig. 7 – Effective normal stress path of specimens with void ratios of 0.75 (left) and 0.80 (right) under Rayleigh wave strain condition I

During the cyclic loads of Rayleigh wave strain condition, the amplitude of the change in mean effective stress also significantly exceeds that under the SHV-wave strain condition. The phenomena can be explained by the initial anisotropy of specimens as follows: The absolute value of the increment or decrement of the normal strain in the *x* and *z*-directions is identical to that under the Rayleigh wave strain condition. However, there are differences in the absolute value of the increment or decrement of effective normal stress in each direction given the anisotropy of specimens induced by K_0-consolidation. Decreases in σ'_z significantly exceed increases in σ'_x, and increases in σ'_z significantly exceed decreases in σ'_x during cyclic loads, as shown in Fig.7. In Fig.7, the change in the color of effective normal stress paths represents the change in σ'_x.

4.3 Liquefaction resistance evaluated via NDE

The accumulated dissipated energy corresponds to *W*, and the increment d*W* is defined as follows [19]:

$$dW = \sigma'_x d\varepsilon_x + \sigma'_y d\varepsilon_y + \sigma'_z d\varepsilon_z + \tau_{xy} d\gamma_{xy} + \tau_{yz} d\gamma_{yz} + \tau_{zx} d\gamma_{zx} \quad (12)$$

where σ'_x, σ'_y, and σ'_z denotes the effective stress in each direction; $d\varepsilon_x$, $d\varepsilon_y$, and $d\varepsilon_x$ denote the normal strain increment in each direction; and $d\gamma_{xy}$, $d\gamma_{yz}$, and $d\gamma_{zx}$ denote the shear strain increment in each plane. The NDE is defined as the accumulated dissipated energy normalized by the initial mean effective stress. It corresponds to an index that represents the liquefaction resistance of specimens in the study.

The NDE consumed during cyclic loads up to the initial liquefaction state under Rayleigh I and Rayleigh

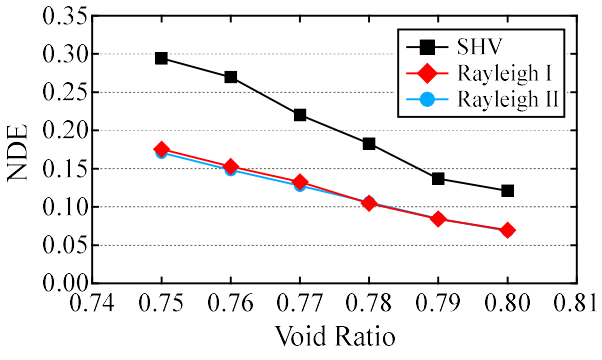

Fig. 8 – NDE consumed during cyclic loads up to the initial liquefaction state

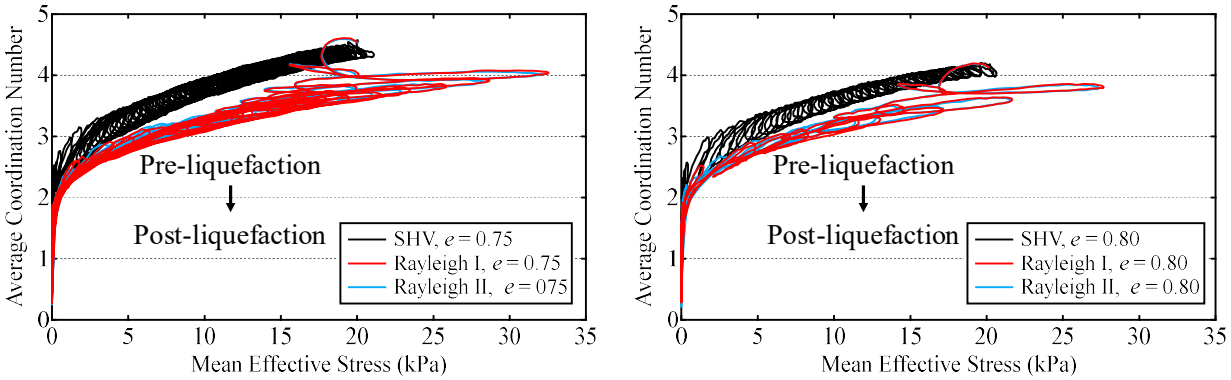

Fig. 9 – Average coordination number of specimens with void ratios of 0.75 and 0.80 during cyclic loads

II is almost identical, which implies that the effect of shear strain component on the liquefaction resistance of specimens is negligible when it is very low when compared to the normal strains. When specimens reach the initial liquefaction state, the NDE of specimens with different void ratios under the SHV-wave strain condition and Rayleigh wave strain condition is shown in Fig.8. Generally, the results indicate that the dense specimen exhibits a higher liquefaction resistance than the loose specimen in the SHV-wave strain condition and Rayleigh wave strain condition. Significantly, specimens under the Rayleigh wave strain condition are significantly more liable to liquefy than that under the SHV-wave strain condition.

4.4 Average coordination number during cyclic loads

The average coordination number corresponds to an important index to represent the microscopic behavior of specimens, and this is related to the stability of the structure system of specimens. The average coordination number corresponds to the average contact number of a particle [20]. As shown in Fig.9, the results indicate that once the average coordination number reaches below 2, the initial liquefaction happens.

The evolution of the average coordination number of specimens under the Rayleigh wave strain condition significantly differs from that under the SHV-wave strain condition. As shown in Fig.9, the average coordination number of the specimen under the Rayleigh wave strain condition decreases rapidly at the initial time, thereby implying that the specimen enters into an unstable state. The average coordination number of the specimen under the SHV-wave strain condition decreased slowly albeit steadily. Therefore, it is concluded that it is easier to destroy the stable structure system of specimens in the Rayleigh wave strain condition than in the SHV-wave strain condition.

5. Conclusions

In the study, a series of simulation tests under the SHV-wave strain condition and Rayleigh wave strain condition were conducted via 3D DEM. The results indicate that the liquefaction behavior under two types of strain conditions is significantly different. The conclusions of the study are summarized as follows:

(1) Under the Rayleigh wave strain condition, the normal strain, which relatively exceeds the shear strain at shallow depths that is liquefiable, corresponds to the dominant factor that affects the liquefaction behavior of specimens.

(2) In the same initial state and with the same accumulated equivalent shear strain in a cycle, the development of pore water pressure in specimens under the Rayleigh wave strain condition is considerably faster than that under the SHV-wave strain condition. Furthermore, the liquefaction resistance of specimens under the Rayleigh wave strain condition is significantly lower than that under the SHV-wave strain condition. The reason is that it is easier to destroy the stable particle structure of specimens in the Rayleigh wave strain condition.

6. References

[1] Trifunac MD (1971): Response envelope spectrum and interpretation of strong earthquake ground motion. *Bulletin of the Seismological Society of America*, **61** (2), 343-356.

[2] Ishihara K (1996). Soil behaviour in earthquake geotechnics.

[3] Fang H, Wang Z, Zao S (1979): Macroscopic mechanism of soil liquefaction and its influence on earthquake damage of ground. Proc. 26*th* Int. Geol. Cong.

[4] Sugano T, Yanagisawa E (1992): Cyclic undrained shear behavior of sand under surface wave stress conditions. *10th World Conference on Earthquake Engineering*, Madrid, Spain.

[5] Cui J, Men F, Wang X (2004): Soil liquefaction induced by Rayleigh wave. *13th World Conference on Earthquake Engineering*. Vancouver, Canada.

[6] Nakai K, Asaoka A, Sawada Y (2016): Liquefaction damage enhanced by interference between the body wave and surface wave induced from the inclined bedrock. *Japanese Geotechnical Society Special Publication*, **2** (19), 723-728.

[7] Noda T, Kazama M, Asaoka A (2017): New developments related to clarification of the mechanisms of ground deformation caused by earthquakes -in the wake of the Great East Japan earthquake. *Journal of JSCE*, **5** (1), 133-144.

[8] Jiang M, Kamura A, Kazama M (2019): Numerical Study on Liquefaction Caused by Love Wave Strain Condition by 3D Discrete Element Method. *In Geotechnics for Sustainable Infrastructure Development*, Hanoi, Vietnam.

[9] Cui J. (2002): Wave propagation and soil liquefaction in aquifers. [D]. Beijing: National Seismological Bureau. (In Chinese)

[10] Cundall PA, Strack OD (1978): *The distinct element methods as a tool for research in granular media*. *Part I*, Report to NSF.

[11] Cundall PA, Strack OD (1979a): A discrete numerical model for granular assemblies. *Géotechnique*, **29** (1), 47-65.

[12] Cundall PA, Strack OD (1979b): *The distinct element methods as a tool for research in granular media. Part II*, Report to NSF.

[13] O'Sullivan C (2011). *Particulate discrete element modelling: a geomechanics perspective*. CRC Press.

[14] Figueroa JL, Saada AS, Liang L, Dahisaria NM (1994): Evaluation of soil liquefaction by energy principles. *Journal of Geotechnical Engineering*, **120** (9), 1554-1569.

[15] Kazama M, Suzuki T, Yanagisawa E (1999): Evaluation of dissipation energy accumulated in surface ground and its application to liquefaction prediction. *Journal of Geotechnical Engineering of JSCE*, **1999** (631), 161-177.

[16] Kokusho T, Mimori Y (2015): Liquefaction potential evaluations by energy-based method and stress-based method for various ground motions. *Soil Dynamics and Earthquake Engineering*, (75), 130-146.

[17] Pujol J (2003): *Elastic Wave Propagation and Generation in Seismology*. Cambridge University Press.

[18] Wei X, Zhang Z, Wang G, Zhang J (2019): DEM study of mechanism of large post-liquefaction deformation of saturated sand. Rock and Soil Mechanics, **40** (4), 1596-1602. (In Chinese)

[19] Zhou Z, Chen G, Huang, C, Chen S (2015): Experimental Study of Liquefaction Characteristics of Saturated Silt Based on the Cumulative Dissipated Energy. *China Earthquake Engineering Journal*, **37** (1), 1-5. (In Chinese)

[20] Thornton C (2000): Numerical simulations of deviatoric shear deformation of granular media. *Géotechnique*, **50** (1), 43−53.

